ARTICLES
https://doi.org/10.1038/s41566-017-0033-z

nature photonics

Corrected: Publisher correction

Chalcogenide glass-on-graphene photonics

Hongtao Lin[1*], Yi Song[2], Yizhong Huang[1,3], Derek Kita[1], Skylar Deckoff-Jones[1], Kaiqi Wang[1], Lan Li[1], Junying Li[1,4], Hanyu Zheng[1], Zhengqian Luo[1,3], Haozhe Wang[2], Spencer Novak[5], Anupama Yadav[5], Chung-Che Huang[6], Ren-Jye Shiue[2], Dirk Englund[2], Tian Gu[1], Daniel Hewak[6], Kathleen Richardson[5], Jing Kong[2] and Juejun Hu[1*]

Two-dimensional (2D) materials are of tremendous interest to integrated photonics, given their singular optical characteristics spanning light emission, modulation, saturable absorption and nonlinear optics. To harness their optical properties, these atomically thin materials are usually attached onto prefabricated devices via a transfer process. Here, we present a new route for 2D material integration with planar photonics. Central to this approach is the use of chalcogenide glass, a multifunctional material that can be directly deposited and patterned on a wide variety of 2D materials and can simultaneously function as the light-guiding medium, a gate dielectric and a passivation layer for 2D materials. Besides achieving improved fabrication yield and throughput compared with the traditional transfer process, our technique also enables unconventional multilayer device geometries optimally designed for enhancing light–matter interactions in the 2D layers. Capitalizing on this facile integration method, we demonstrate a series of high-performance glass-on-graphene devices including ultra-broadband on-chip polarizers, energy-efficient thermo-optic switches, as well as graphene-based mid-infrared waveguide-integrated photodetectors and modulators.

The isolation of single-layer graphene in 2004 triggered intensive investigations into two-dimensional (2D) crystals consisting of one or a few monolayers of atoms. With their remarkable optical properties, these materials have garnered enormous interest for their photonic applications as light emitters[1], modulators[2,3], photodetectors[4,5], saturable absorbers[6] and plasmonic sensors[7]. On-chip integration of 2D materials with photonic devices generally relies on layer transfer, where exfoliated or delaminated 2D membranes are attached onto prefabricated devices[8]. Despite its widespread implementation, the transfer approach has its limitations. When transferring these atomically thin crystals onto a substrate with uneven topology, the 2D materials tend to rupture at the pattern step edges. To circumvent such damage, an additional planarization step is often mandated prior to 2D material transfer, which complicates the process[9–12]. Furthermore, the transferred 2D layer resides on top of the prepatterned devices and only interacts with the optical mode through the relatively weak evanescent waves.

To resolve these issues, an alternative 2D material integration route entails growing an optically thick (comparable to optical wavelength in the medium) film directly on 2D materials and lithographically patterning it into functional photonic devices. Besides improved processing yield and throughput compared to the traditional transfer process, this 'monolithic' approach also offers several critical advantages: it enables accurate alignment of photonic components with 2D material structures (for example, in-plane heterojunctions) with lithographic precision, which is difficult to attain using transfer, it allows flexible placement of 2D material layers inside a photonic structure to maximally enhance light–matter interactions and last but not least, it heralds a truly monolithic, wafer-scale integration process with 2D material systems where catalyst-free, large-area continuous growth on semiconductor or dielectric substrates has been realized (for example, graphene on SiC[13], MoS_2 and $MoTe_2$ on SiO_2/Si[14,15]).

Growth of optically thick dielectric films on 2D materials is not a trivial task, however. Integration on graphene, the archetypal 2D material, epitomizes the challenge. Graphene has a chemically inert surface that makes nucleation and growth of a uniform dielectric film on its surface difficult[16]. Surface modification using ozone[17], NO_2[18], or perylene tetracarboxylic acid[19] catalyses nucleation, albeit at the expense of carrier mobility in graphene. Electron-beam evaporation can form continuous dielectric films (for example, SiO_2 and TiO_2) without surface functionalization, although the harsh deposition environment tends to severely degrade graphene quality (Supplementary Section I). Atomic layer deposition (ALD) has been widely adopted for gate dielectric deposition on graphene[20]; however, growing an optically thick layer using ALD is impractical. Alternatively, plasma-enhanced chemical vapour deposition (PECVD) has been attempted for silicon nitride coating on graphene, although the process requires low-density, low-power plasma with a reduced deposition rate to mitigate plasma damage to the graphene surface[21]. Recently, a simple spin-coating process was devised for direct polymer waveguide modulator fabrication on graphene[22]. Nevertheless, the large modal area in low-index-contrast polymer waveguides limits the resulting device footprint and performance. For other 2D materials, especially less stable ones such as black phosphorous[23], protection of the material's structural integrity from high temperatures, plasma and reactive chemicals imposes additional constraints on the integration process.

Here, we present a generic route for photonic integration of 2D materials using chalcogenide glass (ChG) as the backbone

[1]Department of Materials Science & Engineering, Massachusetts Institute of Technology, Cambridge 02139 MA, USA. [2]Department of Electrical Engineering & Computer Science, Massachusetts Institute of Technology, Cambridge 02139 MA, USA. [3]Department of Electronic Engineering, Xiamen University, Xiamen 361005, China. [4]Key Laboratory of Optoelectronic Technology & System, Education Ministry of China, Chongqing University, Chongqing 400044, China. [5]The College of Optics & Photonics, University of Central Florida, Orlando 32816 FL, USA. [6]Optoelectronics Research Centre, University of Southampton, Southampton SO17 1TW, UK. Hongtao Lin, Yi Song, Yizhong Huang, and Derek Kita contributed equally to this work.
*e-mail: hometown@mit.edu; hujuejun@mit.edu

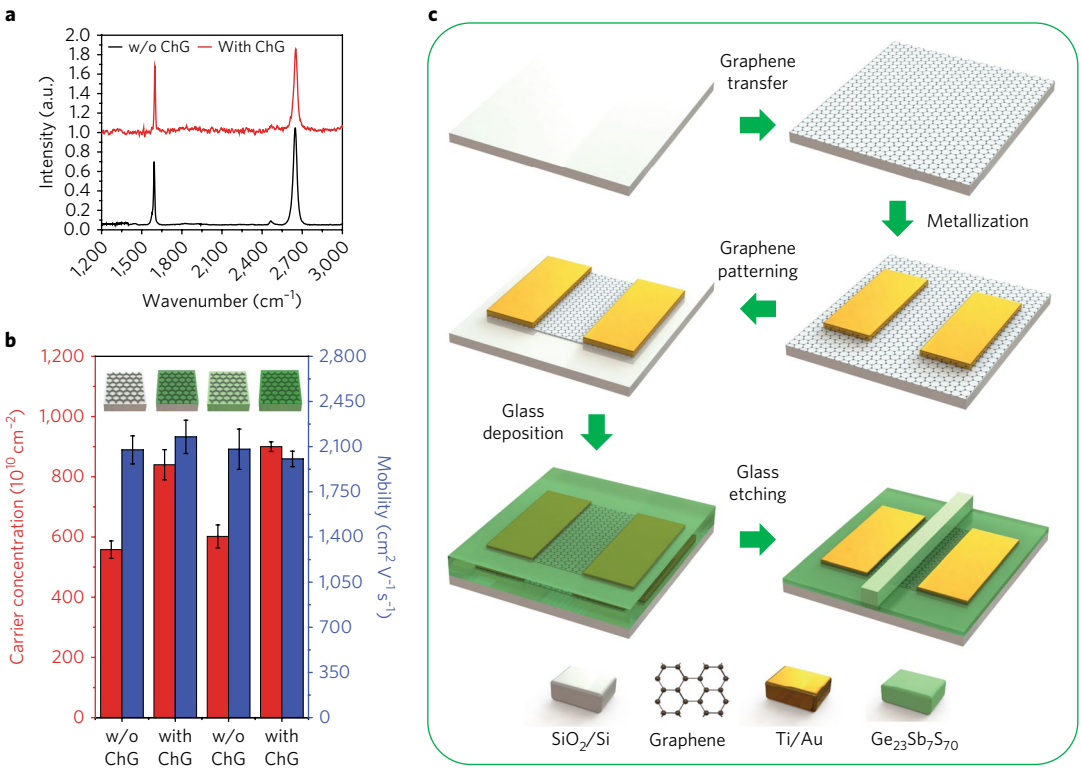

Fig. 1 | Chalcogenide glass–graphene integration. a, Raman spectra of as-transferred monolayer CVD graphene (black) and graphene covered with a $Ge_{23}Sb_7S_{70}$ glass layer (red). Background Raman signal from the $Ge_{23}Sb_7S_{70}$ glass film has been subtracted. **b**, Hall carrier concentration and mobility measured in graphene (results averaged over five samples of each type). From left to right: Graphene transferred onto an oxidized silicon wafer; graphene transferred onto an oxidized silicon wafer and then covered with a $Ge_{23}Sb_7S_{70}$ glass film; graphene transferred onto a $Ge_{23}Sb_7S_{70}$ glass film; graphene sandwiched between two $Ge_{23}Sb_7S_{70}$ glass layers. **c**, Schematic fabrication process flow to integrate chalcogenide glass photonic devices with graphene.

optical material. Chalcogenide glasses, namely the amorphous compounds containing S, Se and/or Te, are emerging photonic materials known for their broadband transparency, high and continuously tunable refractive indices ($n \approx 2$–3.5) and large Kerr nonlinearity[24,25]. In addition to their exceptional optical properties, ChGs are also uniquely poised for 2D material integration. These glasses can be deposited at high rates exceeding 100 nm min^{-1} via simple single-source thermal evaporation with the substrate held near room temperature[26]. Combined with their amorphous nature and good van der Waals adhesion to different substrates without surface modification, the extremely low thermal budget allows epitaxy-free ChG coating with minimal thermal and structural damage to the substrate. Here we show that ChGs can be deposited on a wide variety of 2D materials without disrupting their structure and optoelectronic properties. Figure 1a displays the Raman spectra of monolayer graphene synthesized using CVD before and after coating with a 450-nm-thick thermally evaporated $Ge_{23}Sb_7S_{70}$ ChG film. No defect-related peaks (D, D′ or D+G) were observed after ChG deposition, indicating that the low-temperature glass deposition does not introduce structural defects into graphene[27]. We further confirm that other 2D materials (MoS_2, black phosphorus, InSe and hexagonal BN) similarly remain intact after ChG deposition (Supplementary Section II). Such integration compatibility facilitates the fabrication of unconventional multilayer structures incorporating 2D materials to optimally engineer their interactions with the optical mode. As an example, we exploit the giant optical anisotropy of graphene and modal symmetry in graphene-sandwiched waveguides to demonstrate an ultra-broadband polarizer and a thermo-optic switch with energy efficiency an order of magnitude higher compared to previous reports.

In addition to being an optical guiding medium, the insulating $Ge_{23}Sb_7S_{70}$ glass can function as a gate dielectric and as an effective passivation barrier to prevent 2D materials from degradation inflicted by ambient air, moisture or corrosive chemicals (Supplementary Section III). Figure 1b evaluates the impact of $Ge_{23}Sb_7S_{70}$ glass deposition on transport properties of monolayer CVD graphene transferred onto an oxidized silicon wafer or a $Ge_{23}Sb_7S_{70}$ film on silicon. Notably, despite the increased p-doping (which normally reduces mobility), carrier mobility in graphene remains unchanged after ChG encapsulation, in contrast to most other deposited dielectrics, which tend to degrade carrier mobility due to surface damage during deposition and hence increased defect density[28]. In this Article we harness this feature to demonstrate the first mid-infrared graphene waveguide modulator, where the multifunctional ChG material serves simultaneously as the waveguide and as a gate dielectric to electrostatically modulate the Fermi level in graphene.

Results

Figure 1c illustrates the baseline fabrication protocols for the ChG-on-graphene photonic devices. Details of the fabrication process are provided in the Methods. The following sections present four classes of novel devices leveraging the new integration strategy to reap unique performance benefits. We note that although the devices described herein were fabricated using the specific combination of thermally evaporated $Ge_{23}Sb_7S_{70}$ glass and graphene, we have validated the integration process based on other 2D materials and ChG compositions formed using alternative methods including solution processing and nanoimprint[29] (Supplementary Section IV). The ChG/2D material integration process is therefore generic and can be adapted to meet diverse device design and application needs.

Ultra-broadband on-chip waveguide polarizer. Unlike traditional graphene-integrated devices where the transferred graphene layer is located outside the waveguide core, here we introduce a new multilayer waveguide platform comprising a graphene monolayer situated at the centre of a symmetrically cladded strip waveguide (Fig. 2a). Figure 2c shows a scanning electron microscopy (SEM) image of a fabricated waveguide where a graphene film is sandwiched between two $Ge_{23}Sb_7S_{70}$ layers of equal thickness. The waveguide behaves as a polarizer as a result of the large optical anisotropy of graphene and the polarization-dependent symmetric properties of waveguide modes. To illustrate its working principle, Fig. 2b depicts the electric field components of the fundamental TM (transverse magnetic) and TE (transverse electric) modes supported in the waveguide at a wavelength of 1,550 nm. For TM polarization, its in-plane electric field components (E_x and E_z) are antisymmetric with respect to the centre plane and thus vanish at the graphene layer. Because graphene acts as an optically absorbing metal in-plane and as a lossless dielectric along the out-of-plane direction[30], the waveguide becomes transparent to the TM mode. In contrast, both in-plane electric-field components of the TE mode reach their maxima at the waveguide centre, leading to strong optical attenuation. Using experimental Fermi-level data from Hall measurements, we modelled the propagation losses for the TM and TE modes as 0–1.5 dB cm^{-1} and 575 ± 1.5 dB cm^{-1}, respectively, at a wavelength of 1,550 nm, where the error bars (Fig. 2g) take into account glass thickness deviations based on realistic fabrication tolerances (Supplementary Section V).

To precisely quantify the large polarization-dependent losses in the waveguide, we employed two device structures: ring resonators to characterize the low-loss TM mode and unbalanced Mach–Zehnder interferometers (MZI) to gauge the much higher TE-mode loss. Protocols of loss extraction are summarized in

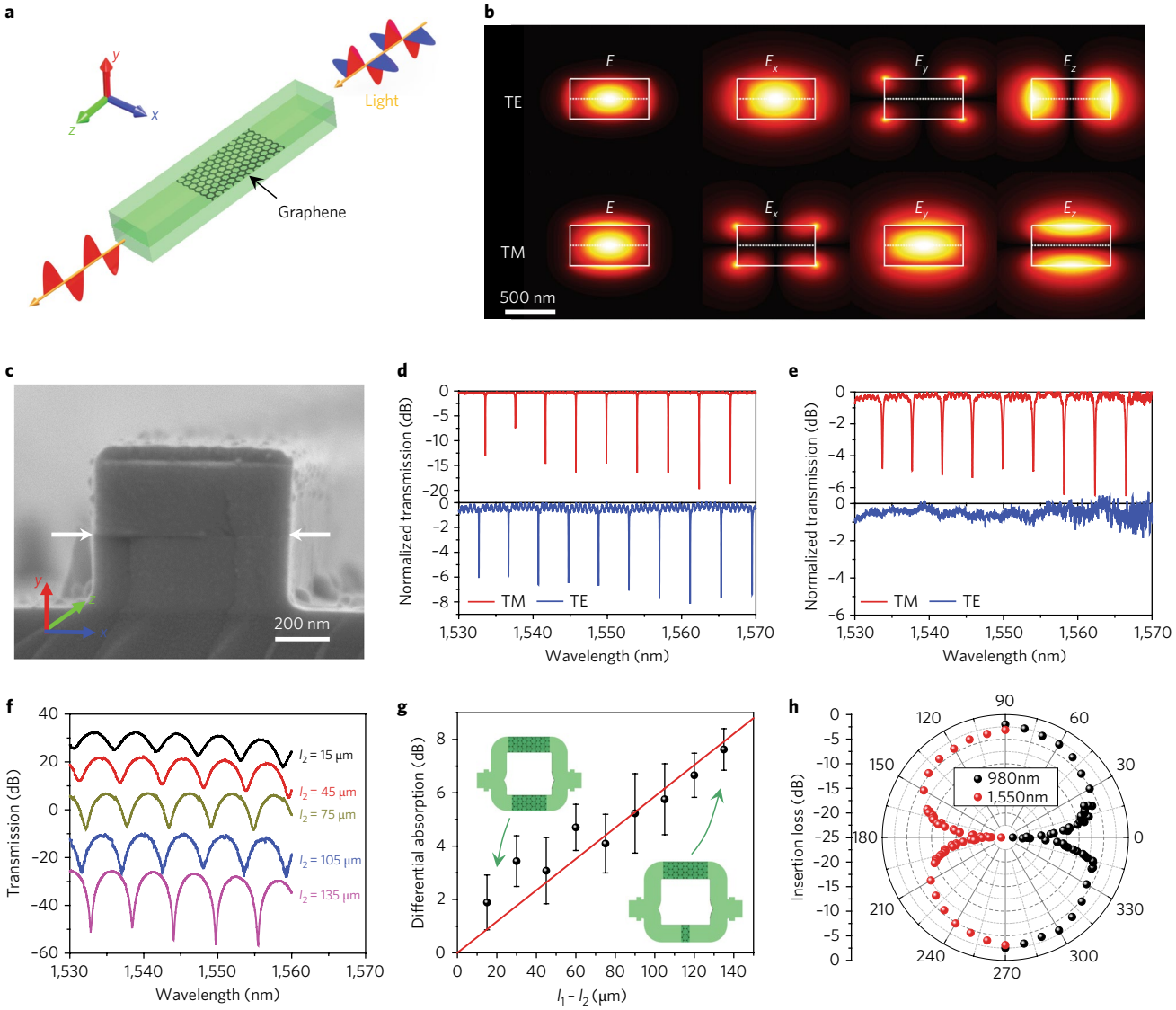

Fig. 2 | Broadband graphene-sandwiched waveguide polarizer. a, Schematic diagram showing the graphene-sandwiched waveguide polarizer. **b**, Simulated modal intensity and electric-field component profiles for fundamental TE and TM modes in the graphene-sandwiched waveguide. **c**, SEM image of the fabricated polarizer cross-section: white arrows mark graphene location. **d**,**e**, Optical transmittance through microring resonators without graphene (**d**) and with embedded graphene (**e**). **f**, Transmittance spectra of unbalanced MZIs with graphene strips of different lengths (l_1 and l_2) embedded in their arms. Here l_1 = 150 mm and l_2 varies from 15 mm to 135 mm. **g**, Differential absorption induced by graphene. Error bars correspond to standard deviations of measurements performed on 10 devices at each l_1–l_2 value. **h**, Polar diagram showing the polarizer performance at 980 nm and 1,550 nm wavelengths. The polar angle represents the angle between the input polarization plane and the substrate.

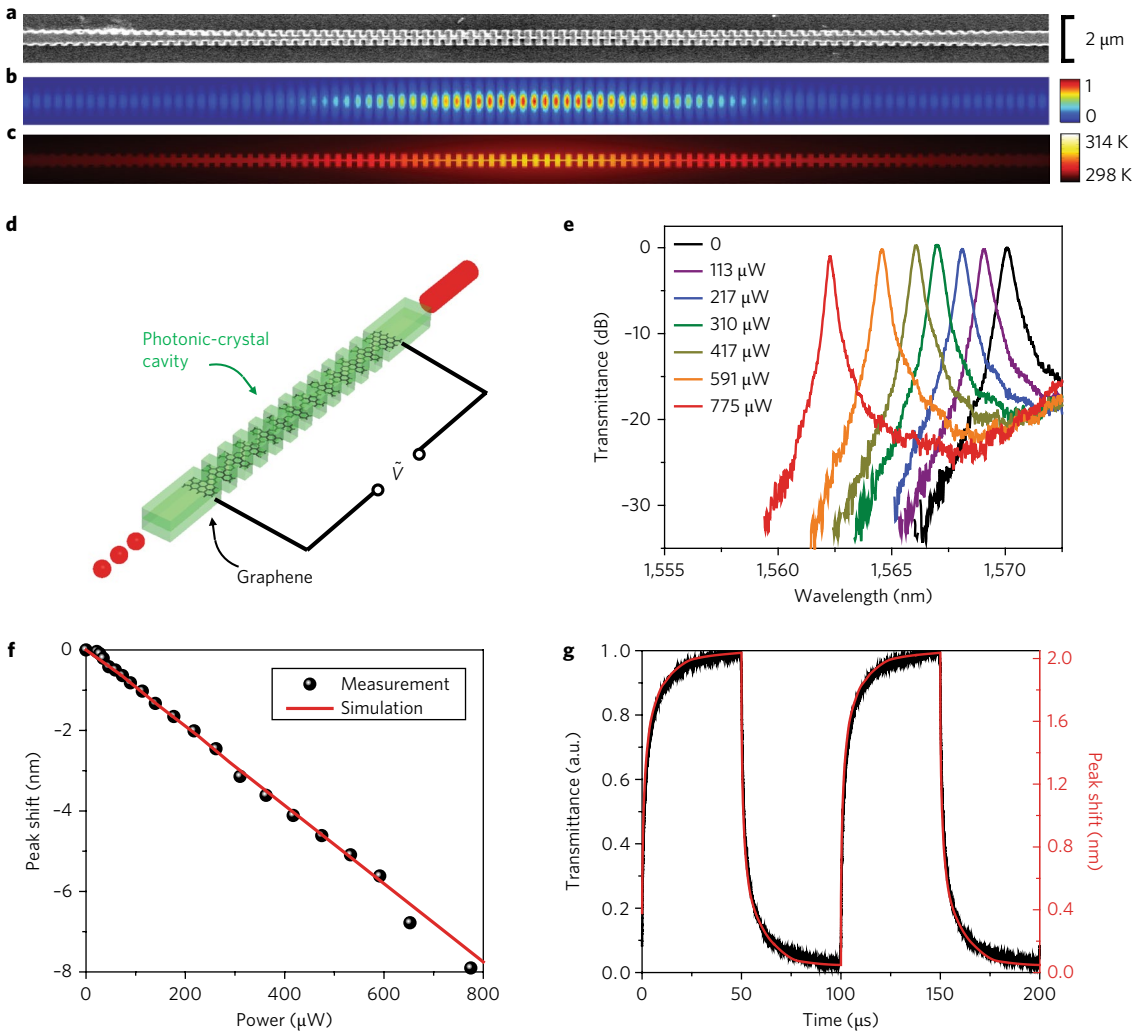

Fig. 3 | Graphene-sandwiched photonic-crystal thermo-optic switch. a, Top-view SEM micrograph of the photonic-crystal thermo-optic switch. **b**, Simulated optical mode profile in the photonic crystal cavity. **c**, Temperature distribution in the device when electric current is flowing through the embedded graphene heater. **d**, Schematic illustration of the thermo-optic switch structure, which consists of a graphene layer embedded in the centre of a photonic-crystal nanobeam cavity. **e**, Optical transmission spectra of the switch at varying input power levels into the graphene heater. **f**, Thermo-optic resonant wavelength shift: the solid line represents finite element method simulation results, whereas the dots are experimental data. **g**, Time-domain response of the switch to a square-wave driving current at 10 kHz.

Supplementary Section VI. Figure 2d,e plots examples of transmission spectra of ring resonators without and with the embedded graphene layer. Although TM-mode resonances are clearly visible for both types of device, the TE-mode resonances disappear in the graphene-sandwiched waveguide, signalling significant TE polarization-selective absorption by graphene. Using the classical coupled-wave transfer matrix formalism, we calculated the excess TM-mode loss induced by graphene to be 20 dB cm^{-1} at 1,550 nm, which we attribute to unevenness of graphene caused by polymer residues from the transfer process (Supplementary Section V). The TE-mode loss was assessed based on the unbalanced MZI transmission spectra in Fig. 2f, where the extinction ratio (ER) of the transmittance undulation correlates with the differential optical attenuation induced by graphene embedded in the MZI arms. Figure 2g plots the calculated differential TE-mode absorption by graphene as a function of embedded graphene length difference in the two arms, from which we infer a TE-mode loss of 590 dB cm^{-1} near 1,550 nm, which agrees well with our theoretical predictions. The results correspond to 23 dB ER and 0.8 dB insertion loss in a 400-μm-long polarizer device operating at 1,550 nm wavelength and a large figure of merit (FOM, defined as the ratio of ER to insertion loss) of 29.

Importantly, because the polarizer design operates on material anisotropy and modal symmetry, both of which are wavelength-independent, the device is broadband in nature. To demonstrate broadband operation of the polarizer, a 400-μm-long polarizer device was characterized at 980 nm and 1,550 nm wavelengths and the results are summarized in the polar diagram in Fig. 2h. The measurement procedures are elaborated in Supplementary Section VII. Consistent with the experimental results, our theoretical model confirms that the same device can operate over a broad spectral range from 940 nm to 1,600 nm with a polarization extinction ratio exceeding 20 dB, which represents the largest operation bandwidth for on-chip waveguide polarizers (Supplementary Section VII).

Energy-efficient photonic-crystal thermo-optic switch. The TM-transparent sandwich waveguide provides an example where graphene is embedded inside a waveguide without incurring excess optical loss. This counterintuitive observation opens up the application of graphene as a broadband transparent heater to realize a

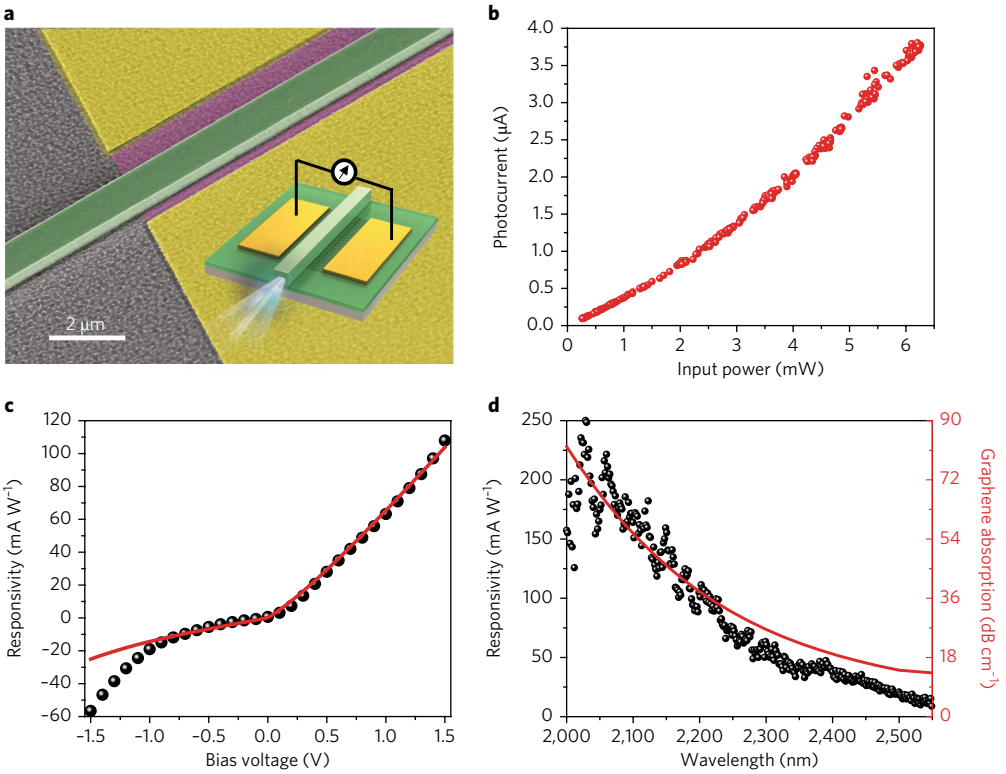

Fig. 4 | Waveguide-integrated graphene mid-infrared photodetector. a, SEM tilted-view micrograph of the mid-infrared waveguide-integrated detector. Inset: Schematic diagram of the device. **b**, Zero-bias photocurrent recorded as a function of input optical power from the waveguide at 2,185 nm wavelength. **c**, Responsivity of the detector device to 2,185 nm waveguide input. **d**, Mid-infrared broadband spectral dependences of the detector's responsivity (at 1.5 V bias) and calculated optical absorption in the graphene layer.

thermo-optic switch with unprecedented energy efficiency. Unlike metal heaters, which have to be placed several micrometres away from the waveguide to suppress parasitic absorption, the waveguide-integrated graphene heater offers superior energy efficiency because of the much smaller thermal mass and large spatial overlap of the optical mode with the heating zone.

Figure 3d schematically illustrates the device structure consisting of a waveguide-coupled photonic-crystal nanobeam cavity formed through depth modulation of side Bragg gratings[31]. A graphene monolayer is embedded in the centre of the nanobeam cavity waveguide and connected to a pair of electrodes as described in Supplementary Section VIII. Figure 3a shows a top-view SEM micrograph of the graphene-embedded nanobeam, which supports a single resonant mode near 1,570 nm (Fig. 3b). When a bias voltage is applied across the electrodes, the graphene and the cavity are resistively heated, leading to a thermo-optic spectral drift of the cavity resonance. Figure 3c depicts the simulated temperature profile as a result of resistive heating in graphene. Because the graphene conductor is placed directly inside the waveguide core, this unique geometry leads to strong thermal confinement and large spatial overlap between the heating zone and the cavity mode, both of which contribute to improved energy efficiency. Figure 3e presents the transmission spectra of the cavity showing progressive resonance detuning with increasing input power. As is shown in Fig. 3f, the measured resonance shift agrees well with our finite element modelling (Supplementary Section IX). The slope of the curve indicates a record energy efficiency of 10 nm mW^{-1}, which represents almost an order of magnitude improvement compared to the best values previously reported in on-chip thermo-optic switches and tuning devices[32].

To elucidate the device physics underlying the exceptional energy efficiency, we analysed the switch's performance characteristics using a lumped element model (Supplementary Section X). A FOM for thermo-optic switches, defined as the inverse of the product of rise time and power consumption, is often cited when drawing comparison between different technologies[33]. With a low switching energy of 0.11 mW and a 10–90% rise time of 14 μs (Fig. 3g), our device features a FOM of 0.65 mW^{-1} μs^{-1}, which is among the highest values reported in an on-chip thermo-optic switch (Supplementary Section XI).

Mid-infrared waveguide-integrated photodetector. Our integration scheme equally applies to optoelectronic devices where graphene becomes the active medium. The broadband infrared transparency of ChGs makes them particularly appealing for integration with graphene, whose zero-gap nature potentially enables broadband optical detection. Our approach simplifies the graphene detector and waveguide integration process through direct deposition and patterning of ChG waveguides and metal contacts on monolayer CVD graphene (Fig. 4a, inset). The device was characterized by launching mid-infrared TE-polarized light into the waveguide and Fig. 4b depicts the detector's photoresponse at zero bias. Three possible mechanisms contribute to photoresponse in graphene: photothermoelectric, photovoltaic (PV) and bolometric effects. To elucidate the origin of the photoreponse, we attempted to fit the data with models for these three response mechanisms (Supplementary Section XIII). The best fit was obtained for the PV mechanism (Fig. 4c). In this fit, the hot carrier relaxation time was taken as a free fit parameter, producing $\tau = 2.3$ ps, in good agreement with directly measured values[34,35]. The increasing responsivity with bias voltage is due to improved carrier collection. The asymmetric shape of the curve is attributed to the off-centred waveguide configuration, as shown in Fig. 4a. The discrepancy of the PV effect for bias < -1 V could be attributed to the difference in

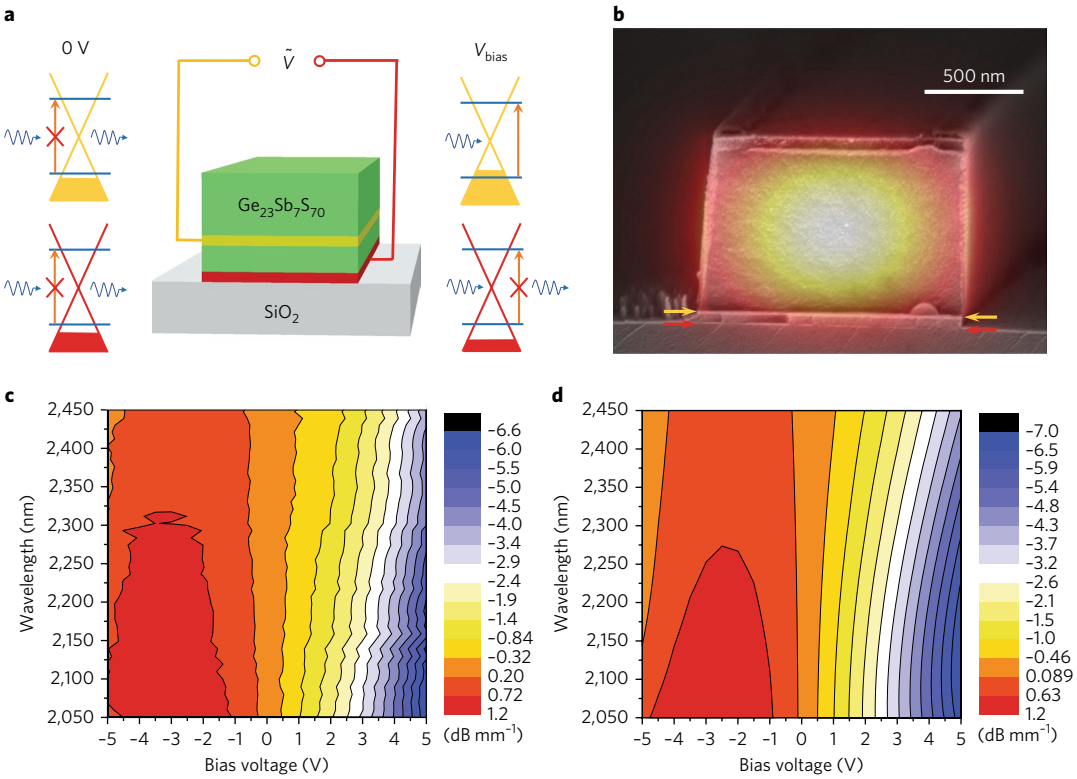

Fig. 5 | Mid-infrared waveguide modulator. a, Centre: Schematic diagram of the mid-infrared waveguide modulator, where the top and bottom graphene layers are labelled with yellow and red colours, respectively. Left and right: Band profiles of the two graphene layers. Brown arrows represent energy of incident photons. **b**, Overlay of simulated TE optical mode profile in the modulator waveguide and an SEM cross-sectional image of the device. Arrows point to the locations of the two graphene layers. **c**,**d**, Measured (**c**) and simulated (**d**) colour contour maps showing wavelength- and bias-dependent modulation depth of the device in dB mm^{-1} (relative to its transmittance at zero bias).

electron and hole mobility[36], which requires further investigation. The device exhibits a broadband photoresponse over the entire scanning range of our tunable laser (2.0–2.55 μm) with a peak responsivity of 250 mA W^{-1} at a wavelength of 2.03 μm (Fig. 4d). The responsivity figure is on par with, or in some cases superior to, state-of-the-art waveguide-integrated graphene detectors operating in the mid-infrared[37] and near-infrared[9,11,38,39]. Hall measurements indicate that the Fermi level of graphene used in the device is located at 0.34 eV below the Dirac point owing to substrate doping[40]. Consequently, the reduced responsivity observed at longer wavelengths manifests the onset of Pauli blocking and decreased optical absorption in the p-type graphene. We modelled the wavelength-dependent absorption in graphene, and the predicted wavelength scaling of graphene absorption is plotted in Fig. 4d. The agreement between the calculated graphene absorption spectrum and the measured responsivity trend validates the hypothesis.

As well as simplifying the integration of graphene detectors with waveguides on silicon, the use of ChGs further opens up photonic integration on unconventional plastic substrates to enable mechanically flexible photonic systems. Leveraging our previously developed flexible substrate integration protocols[41,42], we have demonstrated a waveguide-integrated graphene detector on flexible polymer membranes. Detailed fabrication and characterization outcomes are presented in Supplementary Section XIV.

Broadband mid-infrared waveguide modulator. As previously discussed, the $Ge_{23}Sb_7S_{70}$ glass can function not only as the waveguiding medium, but also as a gate dielectric to control the Fermi level inside graphene. As its Fermi level changes across a threshold value corresponding to half the photon energy, optical absorption of graphene is drastically modified due to Pauli blocking, an effect that has been harnessed to realize near-infrared waveguide modulators[3,43–46] and electro-optic manipulation of free-space mid-infrared light[47–49]. Here, we utilize the versatile ChG material to demonstrate the first graphene-based waveguide modulator operating in the mid-infrared. Figure 5a illustrates the device layout and Fig. 5b shows an overlay of the TE modal profile at 2 μm wavelength and an SEM cross-sectional micrograph of the waveguide. The device working principle is similar to that of double-layer graphene modulators developed by Liu and co-authors[50]. In our case, the active region is formed by two graphene sheets separated by a $Ge_{23}Sb_7S_{70}$ glass gate dielectric of 50 nm in thickness. When a gate bias is applied, charges of opposite signs are electrostatically deposited in the two graphene layers, resulting in shifts of their Fermi levels towards opposite directions. Optical transmission in the waveguide (also made of $Ge_{23}Sb_7S_{70}$ glass) is consequently modulated via Pauli blocking. Using this mechanism, we demonstrate broadband optical modulation for the TE mode across the 2.05–2.45 μm band with modulation depth up to 8 dB mm^{-1}, as shown in Fig. 5c. A thorough theoretical analysis taking into consideration the starting Fermi levels in the two graphene layers as well as Fermi–Dirac carrier distribution is presented in Supplementary Section XV. The theoretically predicted waveguide transmittance as a function of gate bias (Fig. 5d) agrees well with experimental measurements. The current device geometry and our characterization set-up are not optimized for high-speed tests and limit the modulation time constant to 7 μs, being mainly restricted by the large electrical probe capacitance and series resistance. Our calculations show that with improved device design and measurement schemes the attainable modulation bandwidth can be enhanced by five orders of magnitude to

warrant gighertz operation using the same device architecture (Supplementary Section XVI).

Conclusion

In summary, we have established a new paradigm for integrating 2D materials with planar photonic circuits. Unlike traditional methods that rely on post-fabrication transfer, our approach capitalizes on low-temperature ChG deposition to process devices directly on 2D materials without disrupting their extraordinary optoelectronic properties. In addition to streamlining the 2D material integration process, our approach envisages novel multilayer structures with unprecedented control of light–matter interactions in the 2D layers. As an example, we implemented a graphene-sandwiched waveguide architecture to experimentally achieve ultra-broadband on-chip polarization isolation and thermo-optic switching with record energy efficiency. We further leverage the zero-gap nature of graphene to realize ChG waveguide-integrated broadband mid-infrared detectors and modulators, the latter of which also makes use of the multifunctional ChG as the gate dielectric for electrostatic tuning of the Fermi level in graphene. We foresee that the versatile glass-on-2D-material platform will significantly expedite and expand integration of 2D materials to enable new photonic functionalities.

Methods

Methods, including statements of data availability and any associated accession codes and references, are available at https:/doi.org/10.1038/s41566-017-0033-z.

Received: 4 March 2017; Accepted: 27 September 2017;
Published online: 30 October 2017

References

1. Withers, F. et al. Light-emitting diodes by band-structure engineering in van der Waals heterostructures. *Nat. Mater.* **14**, 301–306 (2015).
2. Sun, Z., Martinez, A. & Wang, F. Optical modulators with 2D layered materials. *Nat. Photon.* **10**, 227–238 (2016).
3. Liu, M. et al. A graphene-based broadband optical modulator. *Nature* **474**, 64–67 (2011).
4. Xia, F., Mueller, T., Lin, Y.-m, Valdes-Garcia, A. & Avouris, P. Ultrafast graphene photodetector. *Nat. Nanotech.* **4**, 839–843 (2009).
5. Youngblood, N., Chen, C., Koester, S. J. & Li, M. Waveguide-integrated black phosphorus photodetector with high responsivity and low dark current. *Nat. Photon.* **9**, 247–252 (2015).
6. Bao, Q. et al. Atomic-layer graphene as a saturable absorber for ultrafast pulsed lasers. *Adv. Funct. Mater.* **19**, 3077–3083 (2009).
7. Grigorenko, A., Polini, M. & Novoselov, K. Graphene plasmonics. *Nat. Photon.* **6**, 749–758 (2012).
8. Bonaccorso, F., Sun, Z., Hasan, T. & Ferrari, A. Graphene photonics and optoelectronics. *Nat. Photon.* **4**, 611–622 (2010).
9. Gan, X. et al. Chip-integrated ultrafast graphene photodetector with high responsivity. *Nat. Photon.* **7**, 883–887 (2013).
10. Li, H., Anugrah, Y., Koester, S. J. & Li, M. Optical absorption in graphene integrated on silicon waveguides. *Appl. Phys. Lett.* **101**, 111110 (2012).
11. Schall, D. et al. 50 GBit/s photodetectors based on wafer-scale graphene for integrated silicon photonic communication systems. *ACS Photon.* **1**, 781–784 (2014).
12. Hu, Y. et al. Broadband 10 Gb/s operation of graphene electro-absorption modulator on silicon. *Laser Photon. Rev.* **10**, 307–316 (2016).
13. Nyakiti, L. et al. Enabling graphene-based technologies: toward wafer-scale production of epitaxial graphene. *MRS Bull.* **37**, 1149–1157 (2012).
14. Huang, C.-C. et al. Scalable high-mobility MoS_2 thin films fabricated by an atmospheric pressure chemical vapor deposition process at ambient temperature. *Nanoscale* **6**, 12792–12797 (2014).
15. Zhou, L. et al. Large-area synthesis of high-quality uniform few-layer $MoTe_2$. *J. Am. Chem. Soc.* **137**, 11892–11895 (2015).
16. Colombo, L., Wallace, R. M. & Ruoff, R. S. Graphene growth and device integration. *Proc. IEEE* **101**, 1536–1556 (2013).
17. Lee, B. et al. Characteristics of high-k Al_2O_3 dielectric using ozone-based atomic layer deposition for dual-gated graphene devices. *Appl. Phys. Lett.* **97**, 043107 (2010).
18. Williams, J., DiCarlo, L. & Marcus, C. Quantum Hall effect in a gate-controlled pn junction of graphene. *Science* **317**, 638–641 (2007).
19. Wang, X., Tabakman, S. M. & Dai, H. Atomic layer deposition of metal oxides on pristine and functionalized graphene. *J. Am. Chem. Soc.* **130**, 8152–8153 (2008).
20. Zheng, L. et al. Improvement of Al_2O_3 films on graphene grown by atomic layer deposition with pre-H_2O treatment. *ACS Appl. Mater. Inter.* **6**, 7014–7019 (2014).
21. Zhu, W., Neumayer, D., Perebeinos, V. & Avouris, P. Silicon nitride gate dielectrics and band gap engineering in graphene layers. *Nano Lett.* **10**, 3572–3576 (2010).
22. Kleinert, M. et al. Graphene-based electro-absorption modulator integrated in a passive polymer waveguide platform. *Opt. Mater. Express* **6**, 1800–1807 (2016).
23. Ling, X., Wang, H., Huang, S., Xia, F. & Dresselhaus, M. S. The renaissance of black phosphorus. *Proc. Natl Acad. Sci. USA* **112**, 4523–4530 (2015).
24. Eggleton, B. J., Luther-Davies, B. & Richardson, K. Chalcogenide photonics. *Nat. Photon.* **5**, 141–148 (2011).
25. Ta'eed, V. G. et al. Ultrafast all-optical chalcogenide glass photonic circuits. *Opt. Express* **15**, 9205–9221 (2007).
26. Hu, J. et al. Fabrication and testing of planar chalcogenide waveguide integrated microfluidic sensor. *Opt. Express* **15**, 2307–2314 (2007).
27. Childres, I., Jauregui, L. A., Park, W., Cao, H. & Chen, Y. P. in *New Developments in Photon and Materials Research* (ed. Jang, J. I.) Ch. 19 (Nova Science, New York, 2013).
28. Yang, M., Feng, Y. & Wang, S. in *Graphene Science Handbook: Electrical and Optical Properties* (ed. Aliofkhazraei, M. et al.) 15–24 (CRC Press, Boca Raton, 2016).
29. Zou, Y. et al. Solution processing and resist-free nanoimprint fabrication of thin film chalcogenide glass devices: inorganic–organic hybrid photonic integration. *Adv. Opt. Mater.* **2**, 759–764 (2014).
30. Kwon, M.-S. Discussion of the epsilon-near-zero effect of graphene in a horizontal slot waveguide. *IEEE Photon. J.* **6**, 6100309 (2014).
31. Quan, Q., Deotare, P. B. & Loncar, M. Photonic crystal nanobeam cavity strongly coupled to the feeding waveguide. *Appl. Phys. Lett.* **96**, 203102 (2010).
32. Yu, L., Yin, Y., Shi, Y., Dai, D. & He, S. Thermally tunable silicon photonic microdisk resonator with transparent graphene nanoheaters. *Optica* **3**, 159–166 (2016).
33. Watts, M. R. et al. Adiabatic thermo-optic Mach–Zehnder switch. *Opt. Lett.* **38**, 733–735 (2013).
34. Urich, A., Unterrainer, K. & Mueller, T. Intrinsic response time of graphene photodetectors. *Nano Lett.* **11**, 2804–2808 (2011).
35. Graham, M. W., Shi, S. F., Ralph, D. C., Park, J. & McEuen, P. L. Photocurrent measurements of supercollision cooling in graphene. *Nat. Phys.* **9**, 103–108 (2013).
36. Chen, J. H. et al. Charged-impurity scattering in graphene. *Nat. Phys.* **4**, 377–381 (2008).
37. Wang, X., Cheng, Z., Xu, K., Tsang, H. K. & Xu, J.-B. High-responsivity graphene/silicon-heterostructure waveguide photodetectors. *Nat. Photon.* **7**, 888–891 (2013).
38. Shiue, R.-J. et al. High-responsivity graphene–boron nitride photodetector and autocorrelator in a silicon photonic integrated circuit. *Nano Lett.* **15**, 7288–7293 (2015).
39. Wang, J. et al. High-responsivity graphene-on-silicon slot waveguide photodetectors. *Nanoscale* **8**, 13206–13211 (2016).
40. Goniszewski, S. et al. Correlation of p-doping in CVD graphene with substrate surface charges. *Sci. Rep.* **6**, 22858 (2016).
41. Li, L. et al. Integrated flexible chalcogenide glass photonic devices. *Nat. Photon.* **8**, 643–649 (2014).
42. Zou, Y. et al. High-performance, high-index-contrast chalcogenide glass photonics on silicon and unconventional non-planar substrates. *Adv. Opt. Mater.* **2**, 478–486 (2014).
43. Mohsin, M. et al. Graphene based low insertion loss electro-absorption modulator on SOI waveguide. *Opt. Express* **22**, 15292–15297 (2014).
44. Ye, C., Khan, S., Li, Z. R., Simsek, E. & Sorger, V. J. λ-size ITO and graphene-based electro-optic modulators on SOI. *IEEE J. Sel. Top. Quant.* **20**, 40–49 (2014).
45. Phare, C. T., Lee, Y.-H. D., Cardenas, J. & Lipson, M. Graphene electro-optic modulator with 30 GHz bandwidth. *Nat. Photon.* **9**, 511–514 (2015).
46. Dalir, H., Xia, Y., Wang, Y. & Zhang, X. Athermal broadband graphene optical modulator with 35 GHz speed. *ACS Photon.* **3**, 1564–1568 (2016).
47. Yao, Y. et al. Electrically tunable metasurface perfect absorbers for ultrathin mid-infrared optical modulators. *Nano Lett.* **14**, 6526–6532 (2014).
48. Emani, N. K. et al. Electrical modulation of Fano resonance in plasmonic nanostructures using graphene. *Nano Lett.* **14**, 78–82 (2013).
49. Gao, W. et al. Excitation and active control of propagating surface plasmon polaritons in graphene. *Nano Lett.* **13**, 3698–3702 (2013).
50. Liu, M., Yin, X. & Zhang, X. Double-layer graphene optical modulator. *Nano Lett.* **12**, 1482–1485 (2012).

Acknowledgements

The authors thank L.C. Kimerling and A. Agarwal for providing access to device measurement facilities, Q. Du, P.-c. Shen, W.S. Leong, J. Michon and Y. Zou for assistance with device processing and characterization and M. Mondol for technical support with electron-beam lithography. Funding support is provided by the National Science Foundation under award nos. 1453218, 1506605 and 1509197. This material is based upon work supported by the National Science Foundation Graduate Research Fellowship under grant no. 1122374. R.-J.S. and D.E. gratefully acknowledge funding support by the the Center for Excitonics, an Energy Frontier Research Center funded by the US Department of Energy, Office of Science, Office of Basic Energy Sciences under award no. DE-SC0001088. C.-C.H. and D.H. were funded in part through the Future Photonics Manufacturing Hub (EPSRC EP/N00762X/1). The authors also acknowledge fabrication facility support by the MIT Microsystems Technology Laboratories and the Harvard University Center for Nanoscale Systems, the latter of which is supported by the National Science Foundation under award no. 0335765.

Author contributions

H.L. conceived the device designs and carried out device fabrication and testing. Y.S. prepared and characterized the 2D materials. Y.H. characterized the polarizer and thermo-optic switch devices. D.K. constructed the mid-infrared testing system and measured the detector and modulator devices. S.D.-J. prepared the black phosphorus and InSe samples and performed Raman and passivation tests. K.W. performed numerical modelling of the thermo-optic switch. J.L. and H.Z. deposited the ChG films. S.D.-J., L.L. and Z.L. contributed to device characterization. S.N. and A.Y. synthesized the ChG materials. H.W. and C.-C.H. assisted with 2D material preparation. R.-J.S. assisted in detector design and performed detector device modelling. J.H., T.G., J.K., K.R., D.E. and D.H. supervised and coordinated the research. All authors contributed to technical discussions and writing the paper.

Competing interests

The authors declare no competing financial interests.

Additional information

Supplementary information is available for this paper at https://doi.org/10.1038/s41566-017-0033-z

Reprints and permissions information is available at www.nature.com/reprints.

Correspondence and requests for materials should be addressed to H.L. or J.H.

Publisher's note: Springer Nature remains neutral with regard to jurisdictional claims in published maps and institutional affiliations.

Methods

Device fabrication. Device fabrication was performed at the MIT Microsystems Technology Laboratories and the Harvard Center for Nanoscale Systems. For the mid-infrared detector and modulator, the starting substrate was a silicon wafer coated with 3 µm thermal oxide (Silicon Quest International), whereas for the polarizer and the thermo-optic switch an additional $Ge_{23}Sb_7S_{70}$ layer was deposited onto the wafer before graphene transfer. Monolayer graphene grown using CVD on Cu foils was then transferred onto the substrate following the standard poly(methyl-methacrylate) (PMMA)-based wet transfer process[51]. In all cases, the substrate has a planar surface finish, ensuring a high transfer yield. The graphene layer was subsequently patterned using electron-beam lithography on an Elionix ELS-F125 electron-beam lithography system followed by oxygen plasma etching. Ti/Au (10/50 nm) contact metals were electron-beam evaporated and patterned using PMMA as the liftoff resist. A $Ge_{23}Sb_7S_{70}$ glass film was then deposited via thermal evaporation using a custom-designed system (PVD Products)[26,52]. Small flakes of $Ge_{23}Sb_7S_{70}$ crushed from bulk glass rods prepared using the standard melt quenching technique were used as the evaporation source material[53]. The deposition rate was monitored in real time using a quartz crystal microbalance and was stabilized at 20 Å s^{-1}. The substrate was not actively cooled although the substrate temperature was maintained below 40 °C throughout the deposition as measured by a thermocouple. The $Ge_{23}Sb_7S_{70}$ devices were defined using fluorine-based plasma etching (detailed etching protocols are discussed elsewhere[54]). If needed, the graphene transfer and glass deposition process can be repeated multiple times to create complex multilayer geometries.

Device characterization. The on-chip polarizers were tested using a fibre end-fire coupling scheme and the characterization set-up and protocols are described in detail in Supplementary Section VI. The thermo-optic switch devices were measured on a home-built grating coupling system used in conjunction with an external cavity tunable laser (Luna Technologies) with a built-in optical vector analyser. Laser light was coupled into and out of the devices using single-fibre probes. The d.c. electrical power was supplied and monitored by a Keithley 2401 Source Measure Unit (SMU). For the dynamic test, the a.c. electrical power was provided by a Keysight 33521A function generator while the optical output was recorded on an oscilloscope. The mid-infrared detector and modulator devices were interrogated using a tunable Cr^{2+}:ZnS/Se mid-infrared laser covering wavelengths of 2.0–2.55 µm (IPG Photonics). The mid-infrared laser waveguide coupling and real-time wavelength monitoring system is similar to that described in an earlier publication[55] and is illustrated in Supplementary Section XVII.

Data availability. The data that support the plots within this paper and other findings of this study are available from the corresponding authors on reasonable request.

References

51. Hong, J. Y. et al. A rational strategy for graphene transfer on substrates with rough features. *Adv. Mater.* **28**, 2382–2392 (2016).
52. Musgraves, J. et al. Comparison of the optical, thermal and structural properties of Ge–Sb–S thin films deposited using thermal evaporation and pulsed laser deposition techniques. *Acta Materialia* **59**, 5032–5039 (2011).
53. Petit, L. et al. Compositional dependence of the nonlinear refractive index of new germanium-based chalcogenide glasses. *J. Solid State Chem.* **182**, 2756–2761 (2009).
54. Du, Q. et al. Low-loss photonic device in Ge–Sb–S chalcogenide glass. *Opt. Lett.* **41**, 3090–3093 (2016).
55. Han, Z. et al. On-chip chalcogenide glass waveguide-integrated mid-infrared PbTe detectors. *Appl. Phys. Lett.* **109**, 071111 (2016).